Data-Based Modeling of Vehicle Crash Using Adaptive Neural-Fuzzy Inference System

Lin Zhao, Witold Pawlus, Hamid Reza Karimi, *Senior Member, IEEE*, and Kjell G. Robbersmyr

I. Introduction

THE automotive industry pays exceptional attention to vehicle crashworthiness. Road safety organizations or rating programs like, e.g., Euro NCAP or National Highway Traffic Safety Administration are responsible for executing vehicle crash tests and verifying whether cars satisfy the safety requirements and conform to safety standards. Due to the complexity and cost of the full-scale crash tests, it is advisable to predict and asses the overall car performance without a need to conduct a numerous full-scale experiments. This is being done ultimately to improve the safety of vehicle occupants, since according to [1], e.g., the side impacts are still a serious automotive problem. About 30% of all fatalities for passenger vehicle occupants are caused by this type of collisions. As stated in [2], on U.S. roads, the side impacts are the second cause of death for passenger vehicle users. Between 1980 and 2000, the overall car driver death rate was almost halved in U.S. (see [3]). However, this improvement for the side impact crashes was only by about 24% compared to 52% death rate decline for frontal crashes. This leads to the conclusion that particular attention should be given to modeling and simulation of oblique collisions in order to improve safety of road users involved in this type of accidents.

Finite-element analysis (FEA) is a method that is widely applied in the area of vehicle crash modeling (see [4]–[8]). It offers high accuracy of results and allows for a detailed analysis of interactions between particular vehicle components and environment. The major disadvantages of this approach are high computational power demands of hardware and the fact that it is time consuming. On the other hand, it is also possible to identify only the structural parameters of impacting vehicle and obstacle. In [9] and [10], the lumped parameter models obtained by following this methodology are presented. However, such systems have good degree of fidelity only when used to reproduce collisions similar to the crash scenarios that were used to establish those models. Therefore, in [11] and [12], the application of artificial neural networks and wavelet transform to predict vehicle crash measurements is explored. It was verified that such methodology makes it possible to simulate various crash scenarios. Not only vehicle to barrier collisions are analyzed and modeled to improve road users safety, vehicle to vehicle crashes and motorcycle impacts are discussed as well (see [13] and [14]). A pioneer work in the matter of kinematic synthesis of linkages and associated coordinate systems' description was consolidated and thoroughly discussed in [15]. In [16], the joint coordinates and homogeneous transformations were applied to modeling of vehicle dynamics. Also, in [17], an off-road vehicle ride dynamics model was used to predict vehicle ride vibrations.

The other extremely relevant field of research associated directly with vehicle crash testing is data acquisition. Kalman filtering proves to be an effective tool in data estimation (see [18] and [19]). It is widely applied not only within the area of filtering and signal reconstruction but also for autonomous vehicle control, similarly to H_∞ control (see [20] and [21]).

The adaptive neural-fuzzy inference system (ANFIS) proposed in [26] is one of the most successful neurofuzzy schemes [27], [28], which has been widely used in various scientific domains as a powerful tool of identification, modeling, and control of highly nonlinear mappings. It implements the fuzzy inference mechanism in a connectionist structure, and thus has both the high-level fuzzy reasoning ability and the low-level adaptive learning ability, simultaneously. In [37], the ANFIS approach is used to predict short-term electricity prices in the electricity market of mainland Spain, where particle swarm algorithm has been employed to optimize the parameters of the membership functions. The ANFIS-based estimation is utilized to develop the relationship between the coils' current-response pulsewidths and the active element's position in the proposed sensorless control strategy of a smart-material actuator [29]. The

Manuscript received July 11, 2012; revised November 7, 2012; accepted January 14, 2013. Date of publication April 15, 2013; date of current version February 20, 2014. Recommended by Technical Editor J. Wang.

L. Zhao is with The Ohio State University, Columbus, OH 43210 USA (e-mail: lynchzhao@gmail.com).

W. Pawlus, H. R. Karimi, and K. G. Robbersmyr are with the Department of Engineering, Faculty of Engineering and Science, University of Agder, N-4898 Grimstad, Norway (e-mail: witolp09@student.uia.no; hamid.r.karimi@uia.no; kjell.g.robbersmyr@uia.no).

Color versions of one or more of the figures in this paper are available online.

ANFIS has also been used in [36] to improve the wind energy productivity through directing the turbines toward on the predicted short-term wind vectors. The ANFIS-based controller is designed in [34] to generate acceleration command in the car-following collision prevention system, where the consequent parameters is online updated using a recursive least square algorithm. Moreover, a particle swarm optimization-based fuzzy neural network has been used to control the ball and plate system in [46], the fault detection application of the ANFIS can be found in [22] and [24], and signal processing in [23] and [25]. The theoretical development of the ANFIS has been focused on perspectives such as model structure, high-dimensional inputs, and algorithm efficiency. For instance, a hybrid genetic and singular value decomposition implementation of the ANFIS is proposed for modeling explosive cutting process [35]. Simultaneous reduction of the number of fuzzy rules, training error, and prediction error has been achieved. Liu *et al.* [30] extend the original ANFIS to handle the numerical and categorical inputs together resorting to the firing-strength transform matrix technique. Finally, neural networks serve as an efficient approach to deal with stability issues [31]–[33]. Having observed that the ANFIS has much better accuracy and lower computational needs for modeling complex systems than our previously used methods, it is employed to predict the future crash acceleration signals in this paper. In another word, we establish the nonlinear time-series analysis model for the vehicle crash through the ANFIS architecture. To the best of the authors' knowledge, this problem has not been fully investigated in the past and remains to be important and challenging. This motivates the present study.

The major contribution of this paper is to evaluate the proposed vehicle crash modeling methodology with the wide set of full-scale experimental data. Three different types of collisions are discussed and performance of the created ANFIS is assessed to reproduce kinematics of impacting vehicles. It is verified how the ANFIS established for one set of crash test measurements reproduces crash pulses that are different than the ones used in the ANFIS training stage. Additionally, it is verified how the length of the prediction horizon affects the capability of the ANFIS to simulate a given crash scenario. On top of that, for the type of car to pole collision, the results obtained by ANFIS-based prediction are compared to other methods, which demonstrates a great improvement for the current approach. The motivation for the addressed challenge is worth researching, since the ANFIS-based approach makes it possible to predict behavior of a vehicle involved in a crash scenario. Depending on the length of prediction horizon, one could be able to reconstruct a crash pulse: either partially (what is achieved in this study) or completely. This will allow us to estimate kinematics of a colliding vehicle based on initial values of acceleration which a given vehicle experiences. Ultimately, the methodology discussed might be successfully used to assess impact severity for vehicle occupants without a need to conduct a full-scale crash tests.

The rest of this paper is organized as follows. Section II presents the planar motion dynamic equations for the vehicle, and develops the conversion equation from the local coordinate to the global coordinate. The theoretical background of the ANFIS technique has been elaborated in Section III. Section IV describes the setup of the vehicle crash experiment, where the physical parameters of the experimental vehicles are given. The critical stages of the vehicle collision experiments have been visualized. The analysis of the dynamics of the crash pulses has been given in Section V. Section VI illustrates the application of the ANFIS-based time-series analysis to the modeling of the vehicle crash, and the simulation results are analyzed and compared with those obtained by other methods. Finally, the paper is concluded in Section VII.

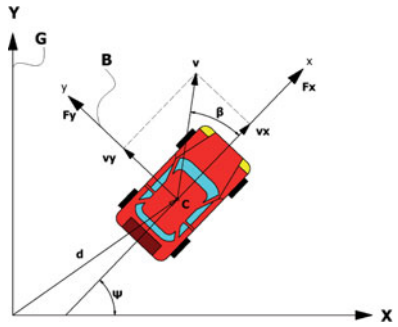

Fig. 1. Rigid vehicle in a planar motion.

II. Rigid Vehicle Dynamics in Planar Motion

Based on [38] and [39], a rigid vehicle has a planar motion with three degrees of freedom (3-DOF): translation in the longitudinal and lateral directions, and a rotation about the vertical axis. In this study, it was decided to follow this assumption and characterize motion of vehicles involved in oblique collisions as a simple 3-DOF case. It is justified since translations in longitudinal and lateral directions of vehicle motion are the ones that affect the overall course of collision (see [40]). The Newton–Euler equations of motion for a rigid vehicle in the body coordinate frame B, attached to the vehicle at its mass center C, are

$$F_x = m\dot{v}_x - m\omega_z v_y \tag{1}$$

$$F_y = m\dot{v}_y + m\omega_z v_x \tag{2}$$

$$M_z = \dot{\omega}_z I_z \tag{3}$$

where F_x is the longitudinal force [N], F_y is the lateral force [N], M_z is the yaw moment [N $\cdot$ m], m is the mass of the vehicle [kg], v_x is the longitudinal velocity component [m/s], v_y is the lateral velocity component [m/s], ω_z is the angular velocity about the vertical axis [rad/s], and I_z is the mass moment of inertia about the vertical axis [kg $\cdot$ m^2].

Fig. 1 illustrates a vehicle in a planar motion. According to [38], a global coordinate frame G is attached to the ground and a local coordinate frame B is attached to the vehicle at the mass center C. The Z- and z-axis are parallel, and the orientation of the frame B is indicated by the heading angle Ψ between the X- and x-axis. The global position vector of the mass center is denoted by d^G.

Due to the fact that typically during a crash a data acquisition system measures local acceleration of a vehicle, in order to

reproduce its behavior, it is necessary to transfer those measurements to the global coordinate system. By following [38], we may find the rigid vehicle's equations of motion in the body coordinate frame by expressing the global equations of motion in the vehicle's body coordinate frame B, using the transformation matrix $\mathbf{R}_{\mathbf{B}}^{\mathbf{G}}$

$$\mathbf{R}_{\mathbf{B}}^{\mathbf{G}} = \begin{bmatrix} \cos\psi & -\sin\psi & 0 \\ \sin\psi & \cos\psi & 0 \\ 0 & 0 & 1 \end{bmatrix}. \tag{4}$$

Similarly, we may apply the transformation matrix to transform the vehicle's local frame coordinates into the coordinates in the global frame. The velocity vector is equal to

$$\mathbf{v}_{\mathbf{C}}^{\mathbf{G}} = \mathbf{R}_{\mathbf{B}}^{\mathbf{G}} \mathbf{v}_{\mathbf{C}}^{\mathbf{B}} \tag{5}$$

or equivalently

$$\begin{aligned} \begin{bmatrix} v_X \\ v_Y \\ 0 \end{bmatrix} &= \begin{bmatrix} \cos\psi & -\sin\psi & 0 \\ \sin\psi & \cos\psi & 0 \\ 0 & 0 & 1 \end{bmatrix} \begin{bmatrix} v_x \\ v_y \\ 0 \end{bmatrix} \\ &= \begin{bmatrix} v_x\cos\psi - v_y\sin\psi \\ v_y\cos\psi + v_x\sin\psi \\ 0 \end{bmatrix} \end{aligned} \tag{6}$$

and therefore, the global acceleration components are calculated as

$$\dot{\mathbf{v}}_{\mathbf{C}}^{\mathbf{G}} = \begin{bmatrix} \dot{v}_X \\ \dot{v}_Y \\ 0 \end{bmatrix} = \begin{bmatrix} (\dot{v}_x - \dot{\psi}v_y)\cos\psi - (\dot{v}_y + \dot{\psi}v_x)\sin\psi \\ (\dot{v}_y + \dot{\psi}v_x)\cos\psi + (\dot{v}_x - \dot{\psi}v_y)\sin\psi \\ 0 \end{bmatrix}. \tag{7}$$

It is noted that according to [40], for a frontal impact when rotation of a vehicle is negligible, it is sufficient to characterize its motion by only using the longitudinal acceleration component. Then, a 2-D motion discussed previously degenerates into 1-D case for which the local longitudinal acceleration is assumed to be the global one ($\dot{v}_X = \dot{v}_x$, $\dot{v}_y = 0$, and $\psi = 0$). Such an approximation is reasonable since it allows us to reproduce an overall behavior of an impacting vehicle.

III. ANFIS Preliminaries

Once the acceleration signals for translation and rotation have been measured, the global acceleration data can be obtained through using the transformation described in the previous section. For a certain type of acceleration signal, we can perform a time-series analysis to it using the ANFIS. This is implemented by using the previous samples of the acceleration signal to predict the later ones in the timeline. The mapping corresponding to this prediction can be characterized by the ANFIS once it has been trained by the data sampled from the acceleration signal. The construction of the training datasets has been elaborated in Section VI. In what follows, we shall focus on the establishment of the ANFIS.

ANFIS is constructed in a similar way to the multilayer feed-forward neural networks. There are usually five layers in a typical ANFIS structure (see, e.g., Fig. 2). In this figure, the ANFIS has two inputs, one output, and two fuzzy rules. The number of nodes in layer 2 determines the number of fuzzy rules. Note that

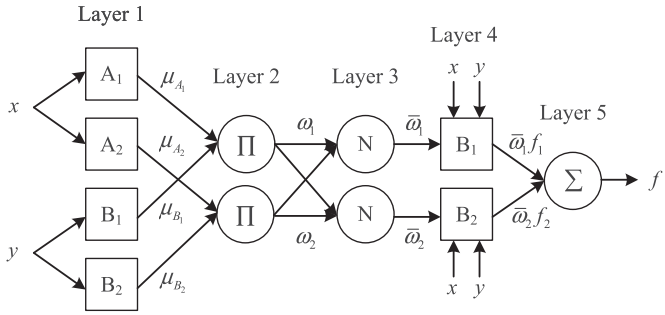

Fig. 2. ANFIS architecture (adapted from [26]).

the square-shaped nodes in Layers 1 and 4 are adaptive nodes, where parameters are adjusted and optimized through the learning process. The circle-shaped nodes in the rest layers are fixed ones and only perform certain types of calculations. For the ith node in the lth layer, we use O_i^l to denote both its output and node functions.

Layer 1 bears the linguistic labels in each node and calculates their corresponding membership grades. The Gaussian type membership function has been adopted in this paper, which is

$$O_i^1 = \mu_{A_i}(x) = e^{-\frac{(x-c_i)^2}{\sigma_i^2}}, \quad i = 1, 2$$

where A_i is the linguistic labels for the first input x. c_i and σ_i are adaptive parameters referred to as the premise parameters. Therefore, we have the output of O_i^1 as the membership degree of x in the fuzzy set A_i.

Layer 2 is a fixed-node layer, where the output of each node represents the firing strength of the corresponding fuzzy rule, which is calculated through taking the minimum value of all the incoming membership grades, i.e.,

$$O_i^2 = \omega_i = \min\left\{\mu_{A_i}(x),\ \mu_{B_i}(y)\right\}, \quad i = 1, 2.$$

It is worth noting that any other triangular norm operator can be applied, for instance, the product operator.

Layer 3 calculates the normalized fire strength of a fuzzy rule, that is, for the ith rule, we have

$$O_i^2 = \bar{\omega}_i = \frac{\omega_i}{\sum_i \omega_i}, \quad i = 1, 2.$$

Layer 4 is comprised of adaptive nodes with node function

$$O_i^4 = \bar{\omega}_i f_i = \bar{\omega}_i(a_{2i}x + a_{1i}y + a_{0i})$$

where $\{a_{0i}, a_{1i}, a_{2i}\}$ is the parameter set for the ith node. These parameters are referred to as the consequent parameters, which can be identified through least square estimation (LSE) or tuned through the gradient descent algorithm. Note that this layer's output is linear in its parameters.

Layer 5 sums all the outputs from layer 4, and therefore, the overall output is

$$O_i^5 = \sum\nolimits_i \bar{\omega}_i f_i.$$

The learning algorithm is diverse. The gradient descent method alone can be used to adjust all the premise and consequent parameters. However, the training process can often

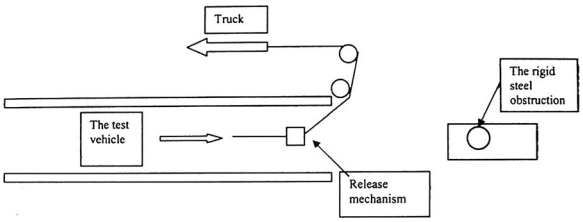

Fig. 3. Scheme of the frontal crash.

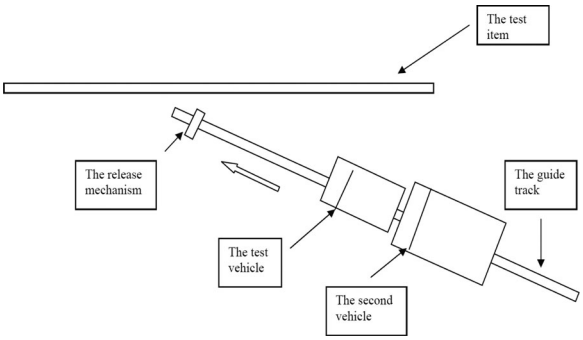

Fig. 4. Scheme of the oblique crash.

run into the local minimum and thus is time consuming. The combination of LSE and gradient descent can significantly accelerate the training process since LSE generates the optimal set of the consequent parameters that minimize the squared error. This hybrid learning algorithm has two passes, which was proposed in [26]. One is the forward pass where the premise parameter is fixed, and the propagation continues until layer 4. The consequent parameters in layer 4 will be identified through LSE based on the outputs of layer 3 and the desired output. Another one is the backward pass where the consequent parameters are fixed, while the error rate is derived in order to update the premise parameters. Apart from that, other optimization algorithm could be embedded into this structure. For example, the parameters can also be obtained through particle swarm optimization [37], genetic algorithm [35], or other evolutionary strategies, which do not require derivative information. However, the tradeoff between computation burden and performance should be considered.

IV. Experimental Setup Description

In this paper, three collisions are described and discussed.

1) Vehicle to pole frontal impact (no.1).
2) Vehicle to safety barrier oblique impact (no.2).
3) Bus to safety barrier oblique impact (no.3).

The layouts of the test setups are shown in Fig. 3 (collision no.1) and Fig. 4 (collisions nos.2 and 3).

During the first two tests (nos.1 and 2—see [41] and [42], respectively), the acceleration at the center of gravity (COG) in three dimensions (x-longitudinal, y-lateral, and z-vertical) was recorded. In a bus to safety barrier collision (no. 3,—see [43]), however, the same measurements were done, but in two locations: two accelerometers were mounted above the bus front and rear axle, respectively. The acceleration was recorded by

Fig. 5. Vehicle no. 1 weighted in tilted position.

using a 3-D accelerometer. The accelerometer was a piezoresistive triaxial sensor with a range of $\pm$1500g. The yaw rate was measured with a gyro instrument, which makes it is possible to record $1^\circ/$s. Data from the sensor were fed to an eight-channel data logger and sampled with a frequency of 10kHz. Table I summarizes the most relevant information regarding each of the collisions.

A. Vehicle COG Determination Procedure

Vehicle COG determination was achieved by weighting each of the vehicles in a horizontal position using four load cells. Afterward, the vehicles were tilted by lifting their frontal parts. The following notations are used: m_1 is the wheel load, front left [kg], m_2 is the wheel load, front right [kg], m_3 is the wheel load, rear left [kg], m_4 is the wheel load, rear right [kg], m_v is the total load (without data acquisition system nor dummy) [kg], m_f is the front mass in tilted position [kg], m_b is the rear mass in tilted position [kg], θ is the angle of tilt [$^\circ$], l is the wheel base [m], d is the distance across the median plane between the vertical slings from the lift brackets at the wheel centers and the load cells [m].

The following formulas were used to determine location of vehicle's COG:

1) *Longitudinal location:* the horizontal distance between COG and the front axle centerline

$$\text{COG}_x = \frac{m_3 + m_4}{m_v} \cdot l. \tag{8}$$

2) *Lateral location:* the horizontal distance between the longitudinal median plane of the vehicle and COG:

$$\text{COG}_y = \frac{m_1 + m_3 - (m_2 + m_4)}{m_v} \cdot \frac{d}{2}. \tag{9}$$

3) *Vertical location:* COG location above a plane through the wheel centers

$$\text{COG}_z = \frac{(m_1 + m_2 - m_f) \cdot l}{m_v \cdot \tan\theta}. \tag{10}$$

The weighing procedure is illustrated in Figs. 5–7. The numerical values obtained are summarized in Tables II–IV.

B. Vehicles—Overall Characteristics

The dimensions of the vehicles are shown in Fig. 8 and listed in Tables V–VII. They represent the two common types of vehicles used in certification of road safety barriers according to [44], namely, small vehicle for test TB11 and bus for test TB51.

Fig. 6. Vehicle no. 2 weighted in tilted position.

Fig. 7. Vehicle no. 3 weighted in tilted position.

TABLE I
CRASH TESTS CONDITIONS

Data	Vehicle *no.* 1: frontal crash	Vehicle *no.* 2: oblique crash	Vehicle *no.* 3: oblique crash
Vehicle mass $[kg]$	873	983	12690
Impact angle ψ $[^\circ]$	0	20	20
Impact velocity $[km/h]$	35	104	72

TABLE II
DATA FOR DETERMINATION OF VEHICLE NO. 1 COG

Parameter	Value	Parameter	Value
m_1 $[kg]$	257	m_v $[kg]$	798
m_2 $[kg]$	237	m_f $[kg]$	444
m_3 $[kg]$	154	m_b $[m]$	354
m_4 $[kg]$	150	θ $[deg]$	28.4
d $[m]$	1.73	l $[m]$	2.28
	COG_x	COG_y	COG_z
Distance $[m]$	0.87	0.03	0.26

TABLE III
DATA FOR DETERMINATION OF VEHICLE NO. 2 COG

Parameter	Value	Parameter	Value
m_1 $[kg]$	235	m_v $[kg]$	819
m_2 $[kg]$	245	m_f $[kg]$	443
m_3 $[kg]$	182	m_b $[kg]$	376
m_4 $[kg]$	157	θ $[deg]$	22.7
d $[m]$	1.71	l $[m]$	2.28
	COG_x	COG_y	COG_z
Distance $[m]$	0.94	0.02	0.25

TABLE IV
DATA FOR DETERMINATION OF VEHICLE NO. 3 COG

Parameter	Value	Parameter	Value
m_1 $[kg]$	2675	m_v $[kg]$	12685
m_2 $[kg]$	2560	m_f $[kg]$	4720
m_3 $[kg]$	3670	m_b $[kg]$	7960
m_4 $[kg]$	3785	θ $[deg]$	19.5
d $[m]$	2.65	l $[m]$	6.65
	COG_x	COG_y	COG_z
Distance $[m]$	3.91	0	0.76

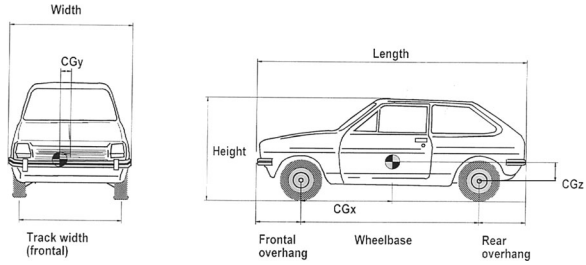

Fig. 8. Characteristic dimensions of the vehicles.

TABLE V
VEHICLE NO. 1 DIMENSIONS (DATA GIVEN IN [m])

Width	Height	Frontal overhang	Wheel track: front axle
1.58	1.39	0.66	1.38
Length	Wheel base	Rear overhang	Wheel track: rear axle
3.64	2.28	0.70	1.34

TABLE VI
VEHICLE NO. 2 DIMENSIONS (DATA GIVEN IN [m])

Width	Height	Frontal overhang	Wheel track: front axle
1.58	1.36	0.63	1.42
Length	Wheel base	Rear overhang	Wheel track: rear axle
3.56	2.28	0.65	1.42

TABLE VII
VEHICLE NO. 3 DIMENSIONS (DATA GIVEN IN [m])

Width	Height	Frontal overhang	Wheel track: front axle
2.50	3.18	2.43	2.10
Length	Wheel base	Rear overhang	Wheel track: rear axle
12.30	6.64	3.23	1.85

Fig. 9. Effect of collision no. 1.

Fig. 10. Subsequent steps of the crash test no. 1.

C. Vehicle no. 1 Frontal Impact—Obstacle

The obstruction and car themselves are shown in Fig. 9. The behavior of the test vehicle was also recorded by using the high-speed cameras—the side view of the collision is illustrated in Fig. 10.

Fig. 11. Effect of collision no. 2.

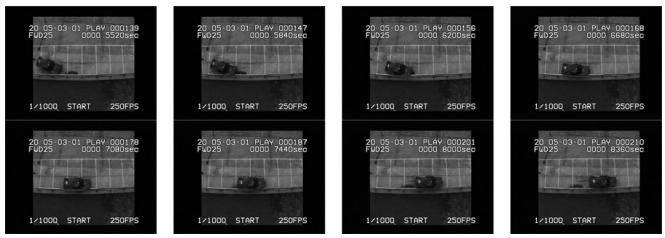

Fig. 12. Subsequent steps of the crash test no. 2.

Fig. 13. Effect of collision no. 3.

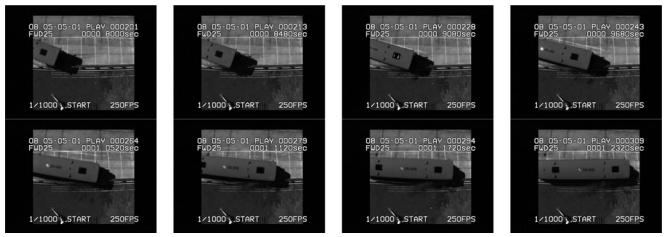

Fig. 14. Subsequent steps of the crash test no. 3.

D. Vehicle nos. 2 and 3 Oblique Impact—Test Items

In both of those collisions, the same type of a road safety barrier was used. In Fig. 11, the vehicle is shown just before and during the impact. Motion of the vehicle throughout the short collision period is illustrated in Fig. 12. Similarly, Fig. 13 visualizes behavior of the bus during the crash test, and Fig. 14 shows particular stages of bus movement in slow motion.

V. Analysis of Crash Pulses

Motion of each vehicle is reconstructed by taking advantage of the acceleration measurements from the collisions.

A. Vehicle no. 1 Frontal Impact

Since it is a central impact, as already mentioned, only the pulse recorded in the longitudinal direction (x-axis) is analyzed.

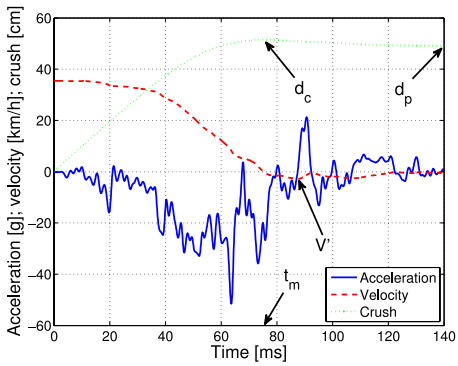

Fig. 15. Vehicle no. 1 kinematics.

TABLE VIII
Relevant Parameters Characterizing Collision no. 1

Parameter	Value
Initial impact velocity V $[km/h]$	35
Rebound velocity V' $[km/h]$	3
Maximum dynamic crush d_c $[cm]$	52
Time when it occurs t_m $[ms]$	76
Permanent deformation d_p $[cm]$	50

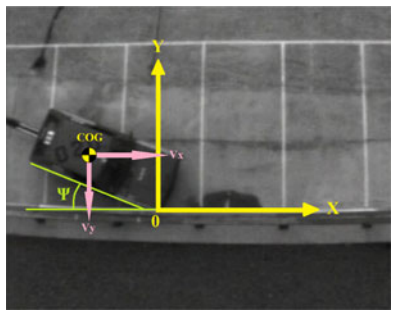

Fig. 16. Vehicle no. 2 moving in the global reference frame.

By integrating car's deceleration, we obtain plots of velocity and displacement, respectively (see Fig. 15). At the time when the relative approach velocity is zero t_m, the maximum dynamic crush d_c occurs. The relative velocity in the rebound phase then increases negatively up to the final separation (or rebound) velocity, at which time a vehicle rebounds from an obstacle. The contact duration of the two masses includes both contact times in deformation and restitution phases. When the relative acceleration becomes zero and relative separation velocity reaches its maximum recoverable value, we have the separation of the two masses. From the crash pulse analysis, we obtain the data listed in Table VIII.

B. Vehicle nos. 2 and 3 Oblique Impact

For this type of collision, only the pulses recorded in the longitudinal (x-axis) and lateral (y-axis) directions together with the yaw rate are analyzed in order to reconstruct the collision—assumed coordinate systems are shown in Fig. 16 for vehicle no. 2 and in Fig. 19 for vehicle no. 3. Using the methodology presented in Section II, the locally measured accelerations and yaw rates allow us to formulate the description of vehicle motion in

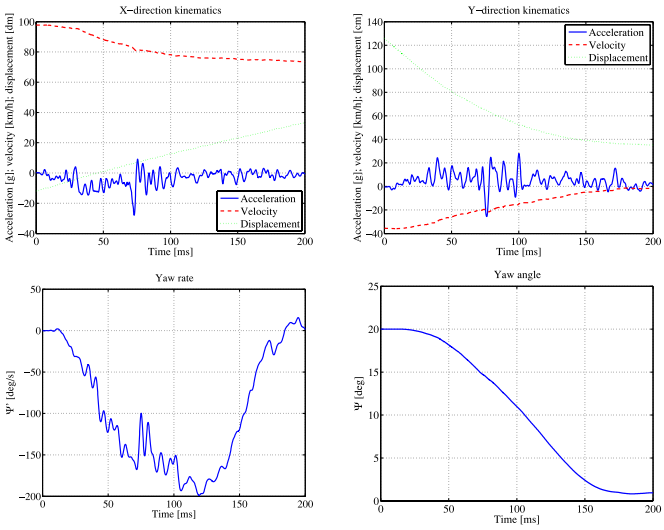

Fig. 17. Kinematics of the experimental vehicle no. 2.

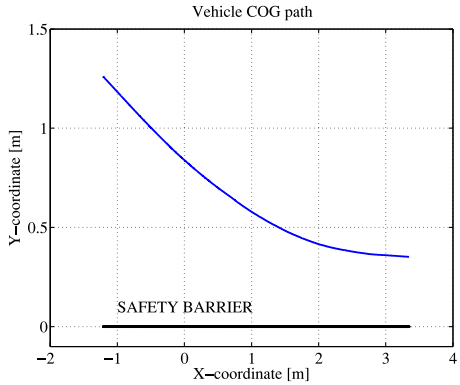

Fig. 18. COG trajectory of vehicle no. 2.

the global reference system. The local kinematics of vehicles is transformed into the global ones by using the relationships given by (7) (see Figs. 17–21). Moreover, the yaw rate and yaw angle are also associated with the global reference frame, instead of the local coordinate system of the vehicle. The particular components (X-longitudinal and Y-lateral, respectively) of the initial velocities are determined by applying a simple trigonometric relationship (initial impact velocity of vehicleno. 2 is $v_{02} = 104$ km/h, vehicle no. 3 is $v_{03} = 72$ km/h, and the angle of impact is $\Psi = 20^{\circ}$)

$$v_{X2} = v_{02} \cdot \cos\Psi = 97.73 \text{ km/h} \tag{11}$$

$$v_{Y2} = v_{02} \cdot \sin\Psi = 35.57 \text{ km/h} \tag{12}$$

$$v_{X3} = v_{03} \cdot \cos\Psi = 67.66 \text{ km/h} \tag{13}$$

$$v_{Y3} = v_{03} \cdot \sin\Psi = 24.63 \text{ km/h}. \tag{14}$$

It is noted that the negative value of the Y-direction velocity component shown in Figs.17–21 is related to the assumed global reference frame (see Figs. 16 and 19). Its center is located directly in the first point of contact between the vehicles and the barrier. The trajectory of COG of vehicle no. 2 during a collision

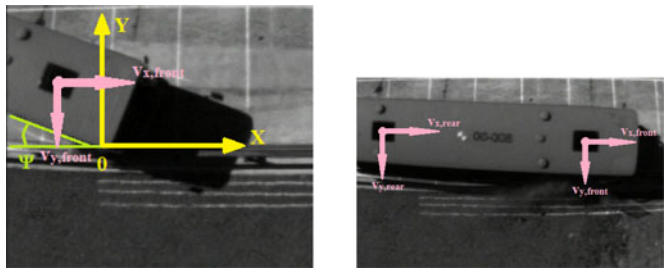

Fig. 19. Vehicle no. 3 moving in the global reference frame.

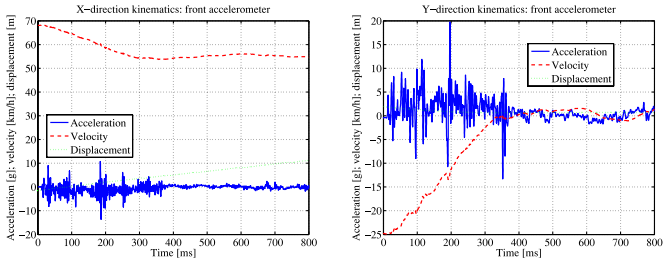

Fig. 20. Kinematics of the front part of the experimental vehicle no. 3.

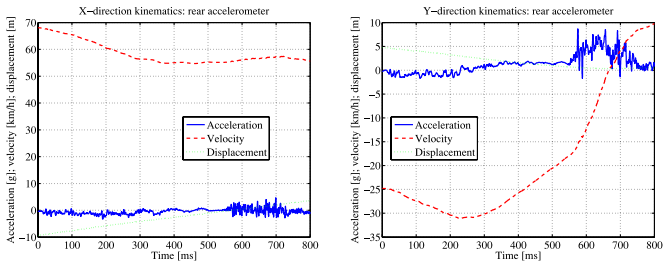

Fig. 21. Kinematics of the rear part of the experimental vehicle no. 3.

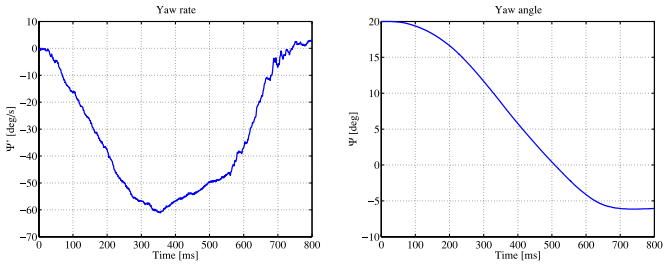

Fig. 22. Yaw rate and angle of the experimental vehicle no. 3.

is shown in Fig. 18. Since for the vehicle no. 3 there are two accelerometers mounted above the wheel axles, it was decided to directly reproduce paths of those two locations, instead of determining position of COG of vehicle no. 3 (see Fig. 23). As far as the bus with safety barrier collision is concerned, in reality, the rotation of the bus around its longitudinal axis is significant—this is visualized by an increase of the absolute value of the lateral velocity component of the rear accelerometer v_Y (see Fig. 21). Moreover, since the two accelerometers installed in vehicle no. 3 are located on its longitudinal centerline and the vehicle is assumed to be rigid, they do experience the same yaw rate shown in Fig. 22, and they have the same initial impact velocities.

TABLE IX
ONE-STEP-AHEAD PREDICTION PERFORMANCE COMPARISON

Training data set: $no.$ 2 collision	Index	A	B	C	D	E	F
X direction	RMSE (g)	0.0191	0.0337	0.0085	-	0.0041	-
Y direction	RMSE (g)	0.0216	-	-	0.0051	-	0.0040

A: Training error B: Test error of no:1 collision.
C: Test error of no:3 collision, front X-acceleration D: Test error of no:3 collision, front Y-acceleration.
E: Test error of no:3 collision, rear X-acceleration F: Test error of no:3 collision, rear Y-acceleration.

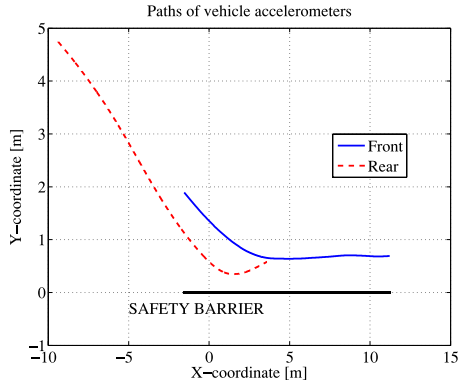

Fig. 23. Trajectories of the front and rear portions of vehicle no. 3.

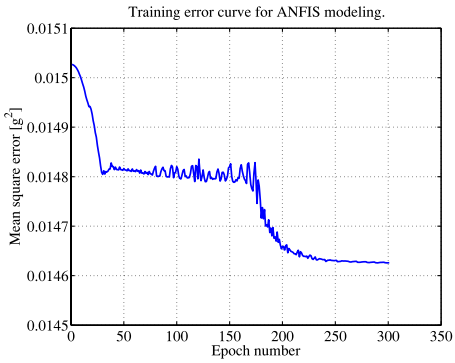

Fig. 24. Training error curves *X*-direction data of three-step-ahead prediction.

VI. SIMULATION RESULTS

First, a three-input, one-step-ahead prediction ANFIS model has been established for reproducing all three types of vehicle crash kinematics. We used the measured acceleration data of collision no. 2 to train the ANFIS. Then, the obtained ANFIS model will be used to reproduce the kinematics of collisions nos. 1 and 3, respectively. Note that the ANFIS trained by *X*-direction data will only be used to predict the collision no. 1 and *X*-direction acceleration of collision no. 3, while ANFIS trained by *Y*-direction data will only be used to predict *Y*-direction acceleration of collision no. 3. The velocity and displacement signals are obtained from the integration of the predicted acceleration signals. The training dataset is extracted in the form of $[x(t-2), x(t-1), x(t), x(t+1)]$, where t is the sample instant. The first three data are inputs and the last one is the output. The number of membership functions for each input is arbitrarily set to 2. Therefore, there are 12 premise parameters, eight fuzzy rules, and 40 consequent parameters. The hybrid learning algorithm using recursive LSE is applied to train the ANFIS. The optimization function is defined as the sum of the squared errors, which is

$$E = \sum_{i=1}^{P} (f_i - \hat{f}_i)^2$$

where f_i is a desired output value, that is the one-step-ahead value of the training data. $\hat{f}_i$ is the corresponding output of the ANFIS. P is the number of training data. Here, we extracted the training dataset from collision no. 2 uniformly, and there are 1998 different entries. The test datasets are constructed in the same way from the acceleration data of collisions nos. 1 and 3, which have 1746 and 7998 entries, respectively. The stop epoch is determined posteriorly by observing the mean square error curves. When squared error E starts to decrease slowly or does not improve over a period of epochs, the training will be stopped. To evaluate the accuracy of ANFIS modeling, we consider the root mean square error (RMSE) as the performance index, which is defined as follows:

$$\text{RMSE} = \sqrt{\frac{1}{P}\sum_{i=1}^{P}(f_i - \hat{f}_i)^2} = \sqrt{\frac{E}{P}}$$

where the unit of RMSE is the gravitational constant g. The simulation results are listed in Table IX, where the second row uses the X-direction acceleration data as the training data, and the third row uses the Y-direction acceleration data. The figures that compare the estimated signals with the measured ones are not shown here because their difference is indiscernible.

Since the performance of the one-step-ahead prediction is quite good, three-step-ahead prediction is performed to measure the potential of the modeling ability of the ANFIS. In this case, the number of inputs is set to four to achieve better results, so the training data is constructed in the form of $[x(t-3), x(t-2), x(t-1), x(t); x(t+3)]$. The training dataset has 1995 entries. The test datasets have 1745 and 7995 entries for the collisions of nos. 1 and 3, respectively. The results have been listed in Table X, which show larger prediction errors than the one-step-ahead prediction. The training error curve of *X*-direction is shown in Fig. 24 and the training performance shown in Fig. 25. Fig. 26 shows the prediction of the car-to-pole collision. Figs. 27 and 28 show the three-step-ahead predictions of the bus-to-barrier collision. *Y*-direction training error, training performance, and the predictions of collision no. 3 are illustrated in Figs. 29–32 respectively.

Moreover, we predict the five-step-ahead acceleration that has the input–output relationship as $[x(t-3), x(t-2), x(t-1), x(t), x(t+5)]$. The training dataset contains 1993 entries. The test datasets contain 1743 and 7993 entries for the collisions nos. 1 and 3, respectively. Table XI shows the simulated RMSE,

TABLE X
THREE-STEP-AHEAD PREDICTION PERFORMANCE COMPARISON

Training data set: $no.$ 2 collision	Index	A	B	C	D	E	F
X direction	RMSE (g)	0.1238	0.2580	0.1441	-	0.0570	-
Y direction	RMSE (g)	0.1359	-	-	0.0664	-	0.0458

*A-F are the same notations as used in Table IX.

TABLE XI
FIVE-STEP-AHEAD PREDICTION PERFORMANCE COMPARISON

Training data set: $no.$ 2 collision	Index	A	B	C	D	E	F
X direction	RMSE (g)	0.3847	0.9605	0.5699	-	0.1878	-
Y direction	RMSE (g)	0.4316	-	-	0.2117	-	0.1591

*A-F are the same notations as used in Table IX.

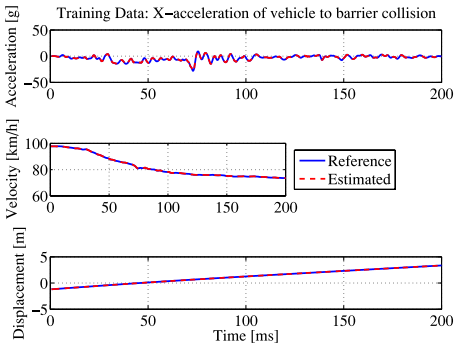

Fig. 25. Training performance *X*-direction data of three-step-ahead prediction.

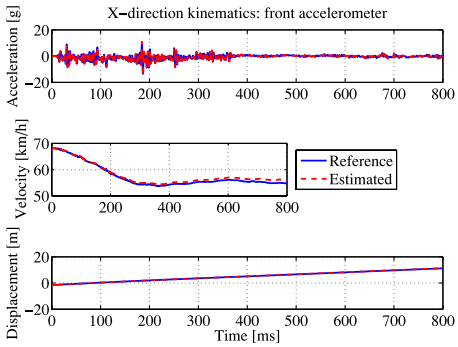

Fig. 27. Three-step-ahead prediction of no. 3 collision, Front *X*.

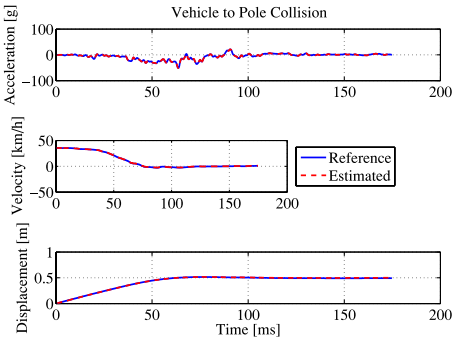

Fig. 26. Three-step-ahead prediction of no. 1 collision.

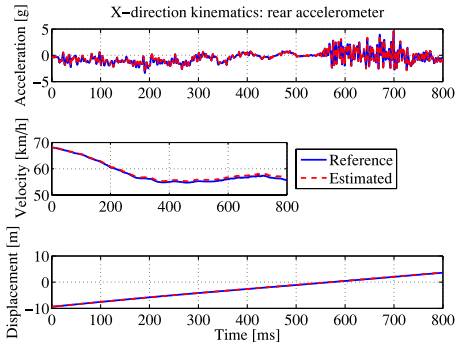

Fig. 28. Three-step-ahead prediction of no. 3 collision, Rear *X*.

which rise up significantly compared to the one-step- and three-step-ahead predictions. Figs. 33–41 demonstrate the training and prediction performances of the ANFIS. Apart from the increasing RMSE index, apparent discrepancy has also been observed as compared with the three-step-ahead prediction, shown in Figs. 36, 37, 40, and 41. Therefore, our simulation stopped at the stage of five-step-ahead prediction.

It can be seen from the tables that the training errors of *Y*-direction are always larger than that of the *X*-direction. And also it can be easily seen from the tables and figures that the less accurate prediction is achieved at longer prediction horizons. It has also been observed in the simulation that the ANFIS can be trained just for a few epochs to have a slightly weaker prediction ability as the optimal ones in terms of the RMSE, because the recursive LSE algorithm always generates the optimal solution and therefore accelerates the training process significantly.This feature facilitates the online application where computation loads should be lowered as much as possible.

In order to visualize the effectiveness of the method presented in this study, the results are compared with the ones presented in [12] and [45]. In [45], vehicle crash was modeled as a viscoelastic system with constant structural parameters. In [12], on the other hand, vehicle crash was reconstructed by the wavelet-based approach. Calculating the RMSEs for each of the methods according to Section VI yields the results shown in Table XII. The value of the RMSE determines the average difference between the reference and estimated value.

As shown in Table XII, the values of RMSE obtained by using the ANFIS-based approach are much lower than the ones calculated from the two other mentioned methods. For the case of car to pole acceleration, the five-step-ahead predictionobtained an RMSE value of 0.9605, as shown in Column B of Table XI. However, the best value in Table XII is 5.22 by the wavelet-based

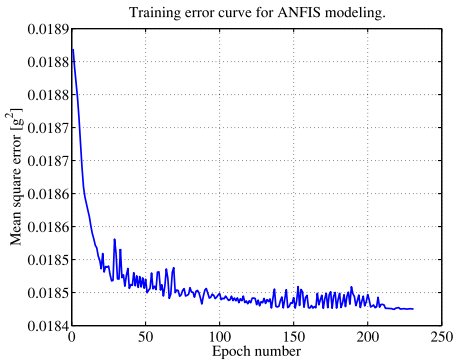

Fig. 29. Training error curves *Y*-direction data of three-step-ahead prediction.

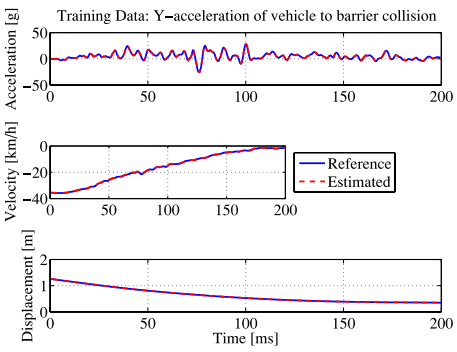

Fig. 30. Training performance *Y*-direction data of three-step-ahead prediction.

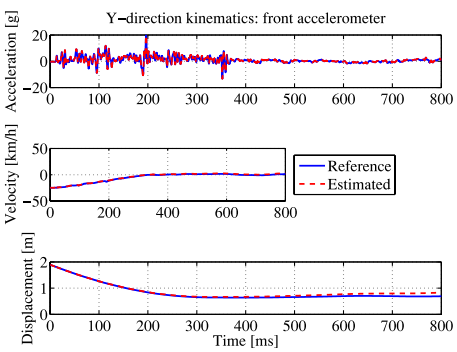

Fig. 31. Three-step-ahead prediction of no. 3 collision, Front *Y*.

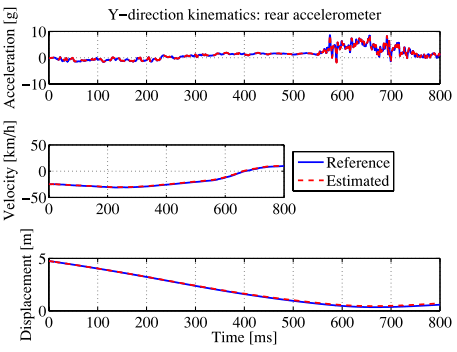

Fig. 32. Three-step-ahead prediction of no. 3 collision, Rear *Y*.

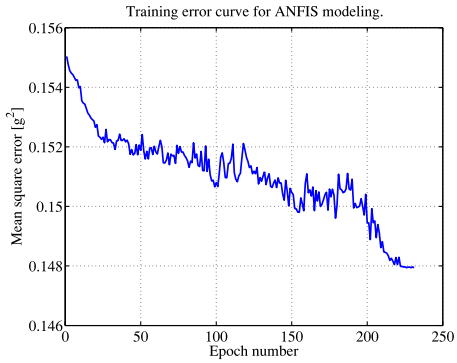

Fig. 33. Training error curves' *X*-direction data of five-step-ahead prediction.

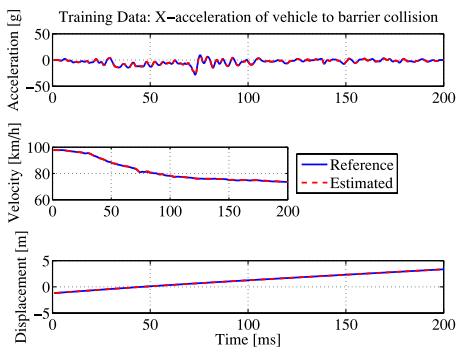

Fig. 34. Training performance *X* direction data of five-step-ahead prediction.

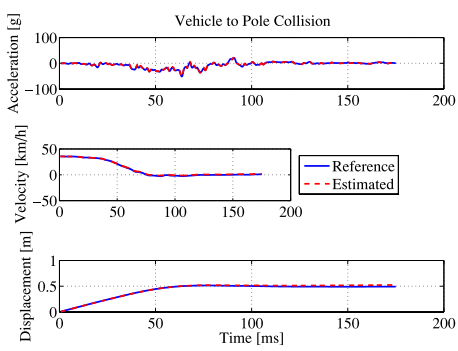

Fig. 35. Five-step-ahead prediction of no. 1 collision.

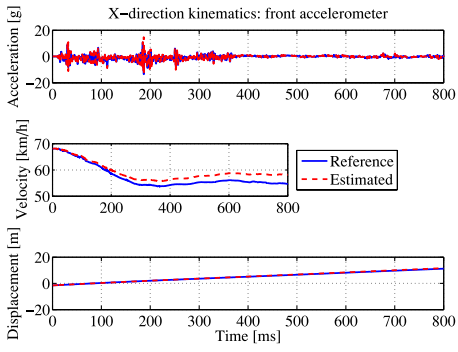

Fig. 36. Five-step-ahead prediction of no. 3 collision, Front *X*.

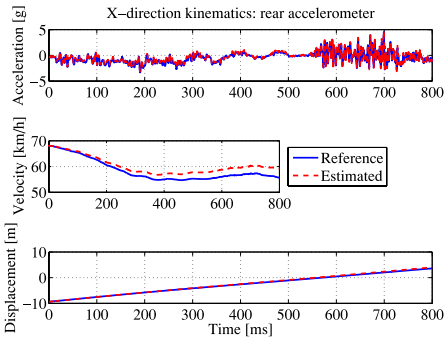

Fig. 37. Five-step-ahead prediction of no. 3 collision, Rear *X*.

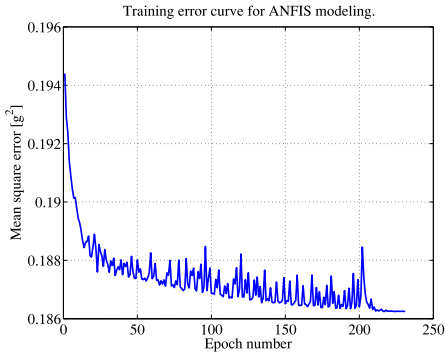

Fig. 38. Training error curves *Y*-direction data of five-step-ahead prediction.

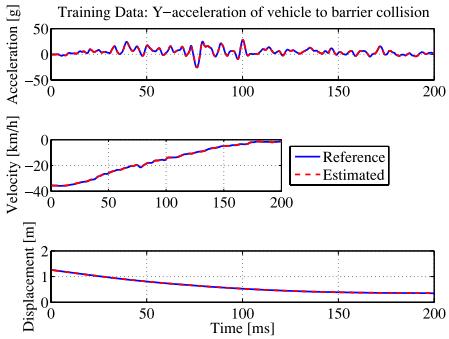

Fig. 39. Training performance *Y*-direction data of five-step-ahead prediction.

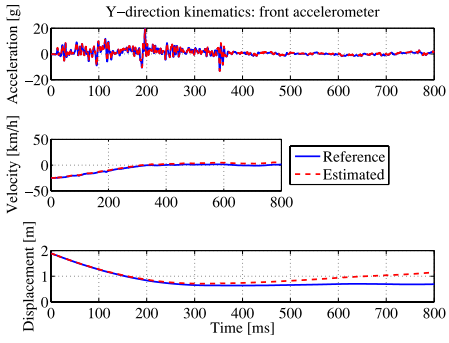

Fig. 40. Five-step-ahead prediction of no. 3 collision, Front *Y*.

signal reconstruction approach, which is much worse than the ANFIS-based prediction approach.

VII. Conclusion

In this paper, three various vehicle collision scenarios were discussed. Motion of the colliding vehicles was approximated to be a pure 3-DOF planar one (oblique crashes) and 1-DOF longitudinal one (frontal impact). Capability of the ANFIS-based method to reconstruct crash pulses of vehicles involved in collisions was investigated. It was verified that by increasing the length of the prediction horizon, less accurate results are obtained. It also affects the computational power which is greater for a longer prediction horizon. It has crucial impact on the modeling and simulation of vehicle crashes since it is of great interest to increase the length of prediction horizon to the extent possible. Additionally, it was examined how the type of crash test data used in the training stage influences the simulation results of the different collision types. The obtained results could be further improved by using a different type of ANFIS structure that would make it possible to extend the length of prediction horizon so that the forecasting capabilities of ANFIS are improved. Consequently, as the prediction horizon is increased, it is advisable to enhance the accuracy of the crash pulse estimation. Finally, it can be used online to forecast the future collision dynamics instead of offline estimating as currently utilized. By achieving this, it would be possible not only to reconstruct a given collision but also to predict how a collision will look like based on updated actual time samples, not just the measured ones.

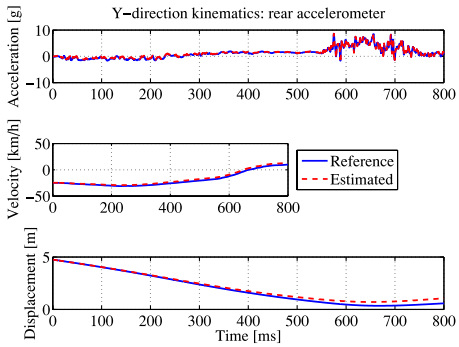

Fig. 41. Five-step-ahead prediction of no. 3 collision, Rear *Y*.

TABLE XII
RMSEs according to [12] and [45]

Quantity	Accel. $[g]$	Vel. $[km/h]$	Disp. $[cm]$
Kelvin model	10.49	16.81	24.60
Maxwell model	8.60	4.02	2.21
Wavelet-based method	5.22	1.15	0.83

References

[1] C. L.-Nadeau, F. Bellavance, S. Messier, L. Vzina, and F. Pichette, "Occupant injury severity from lateral collisions: A literature review," *J. Safety Res.*, vol. 40, no. 6, pp. 427–435, 2009.

[2] Insurance Institute for Highway Safety (IIHS). (2009). Fatality Facts 2009: Occupants of cars, pickups, SUVs, and vans [Online]. Available: http://www.iihs.org/research/fatality_facts_2009/occupants.html

[3] Insurance Institute for Highway Safety (IIHS). (2003). Status Report, Special Issue: Side impact crashworthiness [Online]. Available: http://www.iihs.org/externaldata/srdata/docs/sr3807.pdf

[4] T. Belytschko, "On computational methods for crashworthiness," *Comput. Struct.*, vol. 42, no. 2, pp. 271–279, 1992.

[5] T. L. Tenga, F. A. Chang, Y. S. Liu, and C. P. Peng, "Analysis of dynamic response of vehicle occupant in frontal crash using multibody dynamics method," *Math. Comput. Modell.*, vol. 48, nos. 11–12, pp. 1724–1736, 2008.

[6] Z. Moumni and F. Axisa, "Simplified modelling of vehicle frontal crashworthiness using a modal approach," *Int. J. Crashworth.*, vol. 9, no. 3, pp. 285–297, 2004.

[7] M. Borovinsek, M. Vesenjak, M. Ulbin, and Z. Ren, "Simulation of crash tests for high containment levels of road safety barriers," *Eng. Failure Anal.*, vol. 14, no. 8, pp. 1711–1718, 2007.

[8] W. Barnat, P. Bogusz, P. Dziewulski, R. Gieleta, A. Kiczko, M. Klasztorny, T. Niezgoda, and S. Ochelski, "Experimental validation of the numerical model of a car impact on a road barrier," *J. KONES Powertrain Transp.*, vol. 17, no. 1, pp. 17–27, 2010.

[9] W. Pawlus, H. R. Karimi, and K. G. Robbersmyr, "Mathematical modeling of a vehicle crash test based on elasto-plastic unloading scenarios of spring-mass models," *Int. J. Adv. Manuf. Technol.*, vol. 55, pp. 369–378, 2011.

[10] W. Pawlus, H. R. Karimi, and K. G. Robbersmyr, "Application of viscoelastic hybrid models to vehicle crash simulation," *Int. J. Crashworth.*, vol. 16, no. 2, pp. 195–205, 2011.

[11] W. Pawlus, H. R. Karimi, and K. G. Robbersmyr, "Data-based modeling of vehicle collisions by nonlinear autoregressive model and feedforward neural network," *Inf. Sci.*, vol. 235, pp. 65–79, 2013.

[12] H. R. Karimi, W. Pawlus, and K. G. Robbersmyr, "Signal reconstruction, modeling and simulation of a vehicle full-scale crash test based on Morlet wavelets," *Neurocomputing*, vol. 93, pp. 88–99, 2012.

[13] J. Zhou, H. Peng, and J. Lu, "Collision model for vehicle motion prediction after light impacts," *Veh. Syst. Dyn., Int. J. Veh. Mech. Mobil.*, vol. 46, no. S1, pp. 3–15, 2008.

[14] O. Prentkovskis, E. Sokolovskij, and V. Bartulis, "Investigating traffic accidents: A collision of two motor vehicles," *Transport*, vol. 25, no. 2, pp. 105–115, 2010.

[15] R. S. Hartenberg and J. Denavit, *Kinematic Synthesis of Linkages*. New York, NY, USA: McGraw-Hill, 1964.

[16] M. Szczotka and S. Wojciech, "Application of joint coordinates and homogeneous transformations to modeling of vehicle dynamics," *Nonlinear Dyn.*, vol. 52, no. 4, pp. 377–393, 2008.

[17] A. Pazooki, S. Rakheja, and D. Cao, "Modeling and validation of off-road vehicle ride dynamics," *Mech. Syst. Signal Process.*, vol. 28, pp. 679–695, 2012.

[18] M. Bando, Y. Kawamata, and T. Aoki, "Dynamic sensor bias correction for attitude estimation using unscented Kalman filter in autonomous vehicle," *Int. J. Innovat. Comput., Inf. Control*, vol. 8, no. 3(B), pp. 2347–2358, 2012.

[19] J. Hu, Z. Wang, H. Gao, and L. K. Stergioulas, "Extended Kalman filtering with stochastic nonlinearities and multiple missing measurements," *Automatica*, vol. 48, no. 9, pp. 2007–2015, 2012.

[20] D. Ding, Z. Wang, H. Dong, and H. Shu, "Distributed H_∞ state estimation with stochastic parameters and nonlinearities through sensor networks: The finite-horizon case," *Automatica*, vol. 48, no. 8, pp. 1575–1585, 2012.

[21] Z. Wu, P. Shi, H. Su, and J. Chu, "Reliable H_∞ control for discrete-time fuzzy systems with infinite-distributed delay," *IEEE Trans. Fuzzy Syst.*, vol. 20, no. 1, pp. 22–31, Feb. 2012.

[22] S. Altug, M.-Y. Chen, and H. Trussell, "Fuzzy inference systems implemented on neural architectures for motor fault detection and diagnosis," *IEEE Trans. Ind. Electron.*, vol. 46, no. 6, pp. 1069–1079, Dec. 1999.

[23] K. Assaleh, "Extraction of fetal electrocardiogram using adaptive neuro-fuzzy inference systems," *IEEE Trans. Biomed. Eng.*, vol. 54, no. 1, pp. 59–68, Jan. 2007.

[24] M. S. Ballal, Z. J. Khan, H. M. Suryawanshi, and R. L. Sonolikar, "Adaptive neural fuzzy inference system for the detection of inter-turn insulation and bearing wear faults in induction motor," *IEEE Trans. Ind. Electron.*, vol. 54, no. 1, pp. 250–258, Feb. 2007.

[25] A. Depari, A. Flammini, D. Marioli, and A. Taroni, "Application of an ANFIS algorithm to sensor data processing," *IEEE Trans. Instrum. Meas.*, vol. 56, no. 1, pp. 75–79, Feb. 2007.

[26] J.-S. Jang, "ANFIS: Adaptive-network-based fuzzy inference system," *IEEE Trans. Syst., Man, Cybern.*, vol. 23, no. 3, pp. 665–685, May–Jun. 1993.

[27] F.-J. Lin and R.-J. Wai, "A hybrid computed torque controller using fuzzy neural network for motor-quick-return servo mechanism," *IEEE/ASME Trans. Mechatronics*, vol. 6, no. 1, pp. 75–89, Mar. 2001.

[28] A. Yörükoğlu and E. Altuğ, "Estimation of unbalanced loads in washing machines using fuzzy neural networks," *IEEE/ASME Trans. Mechatronics*, vol. 18, no. 3, pp. 1182–1190, Jun. 2013.

[29] A. Sadighi and W.-J. Kim, "Adaptive-neuro-fuzzy-based sensorless control of a smart-material actuator," *IEEE/ASME Trans. Mechatronics*, vol. 16, no. 2, pp. 371–379, Apr. 2011.

[30] M. Liu, M. Dong, and C. Wu, "A new ANFIS for parameter prediction with numeric and categorical inputs," *IEEE Trans. Autom. Sci. Eng.*, vol. 7, no. 3, pp. 645–653, Jul. 2010.

[31] Z. Wu, P. Shi, H. Su, and J. Chu, "Exponential synchronization of neural networks with discrete and distributed delays under time-varying sampling," *IEEE Trans. Neural Netw. Learn. Syst.*, vol. 23, no. 9, pp. 1368–1376, Sep. 2012.

[32] Z. Wu, P. Shi, H. Su, and J. Chu, "Delay-dependent stability analysis for switched neural networks with time-varying delay," *IEEE Trans. Syst., Man, Cybern. B, Cybern.*, vol. 41, no. 6, pp. 1522–1530, Dec. 2011.

[33] R. Yang, Z. Zhang, and P. Shi, "Exponential stability on stochastic neural networks with discrete interval and distributed delays," *IEEE Trans. Neural Netw.*, vol. 21, no. 1, pp. 169–175, Jan. 2010.

[34] J. Mar and F.-J. Lin, "An ANFIS controller for the car-following collision prevention system," *IEEE Trans. Veh. Technol.*, vol. 50, no. 4, pp. 1106–1113, Jul. 2001.

[35] N. Nariman-Zadeh, A. Darvizeh, and M. Dadfarmai, "Design of ANFIS networks using hybrid genetic and SVD methods for the modelling of explosive cutting process," *J. Mater. Process. Technol.*, vols. 155–156, pp. 1415–1421, 2004.

[36] C. Potter and M. Negnevitsky, "Very short-term wind forecasting for Tasmanian power generation," *IEEE Trans. Power Syst.*, vol. 21, no. 2, pp. 965–972, May 2006.

[37] H. Pousinho, V. Mendes, and J. Catalão, "Short-term electricity prices forecasting in a competitive market by a hybrid PSO-ANFIS approach," *Int. J. Electr. Power Energy Syst.*, vol. 39, no. 1, pp. 29–35, 2012.

[38] R. N. Jazar, *Vehicle Dynamics: Theory and Application*. New York, NY, USA: Springer-Verlag, 2008.

[39] H. Lee and S. Jung, "Balancing and navigation control of a mobile inverted pendulum robot using sensor fusion of low cost sensors," *Mechatronics*, vol. 22, no. 1, pp. 95–105, 2012.

[40] M. Huang, *Vehicle Crash Mechanics*. Boca Raton, FL, USA: CRC Press, 2002.

[41] K. G. Robbersmyr, "Calibration test of a standard Ford Fiesta 1.1l, model year 1987, according to NS-EN 12767," Agder Research, Grimstad, Norway, Tech. Rep. 43/2004, 2004.

[42] K. G. Robbersmyr and O. K. Bakken, "Impact test of safety barrier, test TB 11," Agder Research, Grimstad, Norway, Project Rep. 24/2001, 2001.

[43] K. G. Robbersmyr and O. K. Bakken, "Impact test of safety barrier, test TB 51," Project Rep. 25/2001, Agder Research, Grimstad, Norway, Project Rep. 24/2001, 2001.

[44] *Road Restraint Systems—Part 2: Performance Classes, Impact Test Acceptance Criteria and Test Methods for Safety Barriers*, European Standard EN 1317-2:1998, 1998.

[45] W. Pawlus, H. R. Karimi, and K. G. Robbersmyr, "Development of lumped-parameter mathematical models for a vehicle localized impact," *J. Mech. Sci. Technol.*, vol. 25, no. 7, pp. 1737–1747, 2011.

[46] X. Dong, Y. Zhao, Y. Xu, Z. Zhang, and P. Shi, "Design of PSO fuzzy neural network control for ball and plate system," *Int. J. Innov. Comput. Inf. Control*, vol. 7, no. 12, pp. 7091–7103, 2011.